Synthesis, Structure and Magnetic Characterization of Orthoferrite $LaFeO_3$ Nanoparticles

Yehia M. Abbas, Ahmed B. Mansour, Shehab E. Ali, Ahmed H. Ibrahim*

Physics Department, Faculty of Science, Suez Canal University, Ismailia, 41522, Egypt

Ymabbas@live.com, Shehab_ali@science.suez.edu.eg

Ahmed_Abdel-Hamid@science.suez.edu.eg

ABSTRACT

Single-phase lanthanum orthoferrite ($LaFeO_3$) was prepared by an auto-combustion method. The analysis of synchrotron room temperature X-ray diffraction (XRD) data confirmed the orthorhombic $LaFeO_3$ perovskite of space group Pnma without any impurity phase. The Scherrer's formula and Williamson-Hall plot based on XRD data were employed to estimate the crystallite size of the prepared sample. For a deeper insight into the crystal structure, high-resolution transmission microscopy imaging (HRTEM) was performed. The estimated values of crystallite size from HRTEM and synchrotron XRD data were coincident. The HRTEM images confirmed the polycrystalline nature of the prepared sample through the obvious lattice planes which are related to (121) plane. Furthermore, the M(H) hysteresis loop of the investigated sample was characterized by a vibrating sample magnetometer (VSM). The magnetic properties obtained through analyzing the magnetization versus temperature M(T) and magnetization verses magnetic field M(H) curves indicated that $LaFeO_3$ possessed weak ferromagnetism at room temperature.

Keywords: Auto-combustion method; Rietveld refinement; ELETTRA Synchrotron; TEM; VSM.

SUBJECT CLASSIFICATION

Applied crystallography

Date of Submission: 30 September, 2018

DOI: 10.24297/jap.v14i3.7693

ISSN: 2347-3487

Volume: 14 Issue: 3

Journal: Journal of Advances in Physics

Website: https://cirworld.com

1. INTRODUCTION

Multiferroics are a group of smart materials that display ferroelectric and magnetic properties in a single phase; these materials are considerably rare compared to conventional classes of compositions. Rare-earth perovskites with orthorhombic structures have fascinated both technologists and scientists owing to their exciting and unique chemical and physical properties [1,2] and their wide-ranging applications in solid oxide fuel cells [3], catalysis [4,5], gas sensing [6] and environmental monitoring [7]. Furthermore, improved perovskite compositions, such as $La_{1-x}Sr_xMnO_3$, $La_{0.7}Sr_{0.3}Mn_{1-x}Ni_xO_3$, $CaMn_{1-x}Fe_xO_3$, $Ca_{1-x}Nd_xMnO_3$, $La_{1-x}Pr_xMnO_3$, and others [8–14], have received increasing attention because of their exciting technological applications in magnetic field sensors and actuators.

In $LaFeO_3$, the 3d electrons configuration contributes to magnetic ordering of the transition metal ions within the material, resulting in lattice distortion due to the creation of a strong local electric field. Due to this locally induced field, a ferroelectric arrangement is developed in this type of material. A large number of perovskite structural compositions have been found to possess a large range of spin ordering (ferro/ferrimagnetic and/or antiferromagnetic materials), and dipole moments have been detected [15]. Among the rare-earth perovskites, lanthanum orthoferrite ($LaFeO_3$) is a famous antiferromagnetic composition with a high Néel temperature (T_N~740 °C) [16,17] and possesses a distorted perovskite structure with a Pbnm (or Pnma) space group (SG) [18,19] due to tilting of the octahedral [FeO_6] units. Furthermore, this perovskite possesses high thermal stability and a well-defined structure. These interesting properties have allowed this material to be applied in a number of progressive technologies worldwide. Overall, orthorhombic structured $LaFeO_3$ shows G-type weak antiferromagnetic ordering below 735 K and transitions to ferroelectric ordering at 475 K [20].

In the present study, nano-synthesized $LaFeO_3$ was prepared using a citrate-nitrate auto-combustion technique. In addition to determining the particle size using different methods, the structure, microstructure, and magnetic properties of perovskite $LaFeO_3$ are investigated by means of synchrotron XRD and vibrating sample magnetometer (VSM).

2. Experimental

2.1 Material and methods

Monophase $LaFeO_3$ was prepared using a citrate-nitrate auto-combustion method. Analytical grade $La(NO)_3{\cdot}6H_2O$ and $Fe(NO_3)_3{\cdot}9H_2O$ were used as starting materials, and citric acid monohydrate $C_6H_8O_7{\cdot}H_2O$ was used as a fuel. The metal nitrates were discretely dissolved in distilled water and then mixed together under constant stirring. The metals to citric ratio were maintained at 1:1. The solution was evaporated at 80 –100 °C with continuous stirring using a magnetic stirrer, and the pH was controlled by dropwise adding a proper amount of ammonia solution during the stirring process (pH=7).

Nanocrystalline $LaFeO_3$ was obtained by decomposing the dried gel at a temperature of 300 °C in open air, and finally, a dark yellow powder was obtained after an intense exothermic combustion reaction.

$$La(NO_3)_3{\cdot}6H_2O + Fe(NO_3)_3{\cdot}9H_2O + 2C_6H_8O_7{\cdot}H_2O \xrightarrow{(pH=7)\text{ in open air}} LaFeO_3 + 12CO_2 + 2N_2 + 2NO_2 + 25H_2O$$

2.2 Characterization Techniques

The phase identification and crystal structure of the nano-synthesized $LaFeO_3$ were analyzed using Synchrotron room temperature XRD. The Synchrotron XRD measurements were carried out in transmission mode at MCX beamline of ELETTRA Synchrotron, Trieste, Italy. A beam wavelength of λ = 0.7 Å from Si (111) double-crystal monochromator in non-dispersive configuration was employed, followed by a toroidal focusing mirror with a horizontal acceptance of 2.8 mrad, the diffraction patterns with sample to detector distance of 120 mm. Two dimensional powder diffraction data were transformed into one dimensional pattern (2θ versus intensity) by employing Fit2D. The Instrumental Profile Function of MCX was experimentally determined analyzing the LaB_6 line profile standard, using borosilicate glass capillaries (0.3 mm diameter) in the traditional Debye-Scherrer's

geometry. The optics of the beamline produce X-rays with energy between 4 and 21 keV.

The Rietveld refinement of the XRD peaks was analyzed through the FullProf program. The background was defined selecting several points from the data which were refined concurrently with other structural and profile parameters. The average crystallite size was calculated by the Scherrer's formula taking in to account the integral breadth of the diffraction peaks in the XRD pattern, and a Williamson-Hall plot was used to calculate the particle size and microstrain. Magnetic measurements were performed using a vibrating sample magnetometer (VSM 7310, Lake Shore) in an applied magnetic field of ±20 kOe at room temperature. The shape, morphology and electron diffraction of the fine particles were analyzed using high-resolution transmission electron microscopy (HRTEM) (JEOI-JEM 2100 instrument).

3. Analysis Method

3.1 Rietveld Analysis of XRD data

In the current study, we assumed the Rietveld's powder structure refinement analysis [21-23] of the synchrotron XRD data to refine the structural parameters (lattice parameters, atomic coordinates, thermal parameters and occupancies) and microstructural parameters (average crystallite size and microstrain). For instrumental broadening correction, a specially treated LaB_6 standard [24] was used. FullProf software was used to concurrently refine both the structural and microstructural parameters. In the structural analysis, a Thompson-Cox-Hastings pseudo-Voigt function was used to describe the peak shapes.

3.2. Crystal Structure Refinements

A complete explanation of the mathematical procedures carried out in the Rietveld analysis has been described elsewhere [25-31]. The improvement of the minimization was detected through the usual agreement factors, R_{wp} (weighted residual factor) and R_{exp} (expected residual factor). Additionally, we calculated the so-called goodness of fit (GoF) factor [28-31]:

$$GoF = \frac{R_{wp}}{R_{exp}} \quad (1)$$

Refinement was carried out until convergence was obtained and the GoF factor approached 1.

4. Results and Discussion

4.1. XRD Pattern Analysis

Fig.1 shows the room temperature synchrotron XRD pattern of $LaFeO_3$ prepared by the citrate auto-combustion technique. Peaks corresponding to the (101), (121), (220), (202) and (123) planes were observed, confirming the formation of a pure $LaFeO_3$ phase with a well-defined orthorhombic structure (SG Pnma (62), coinciding with JCPDS: 88-0641) without any impurity phase.

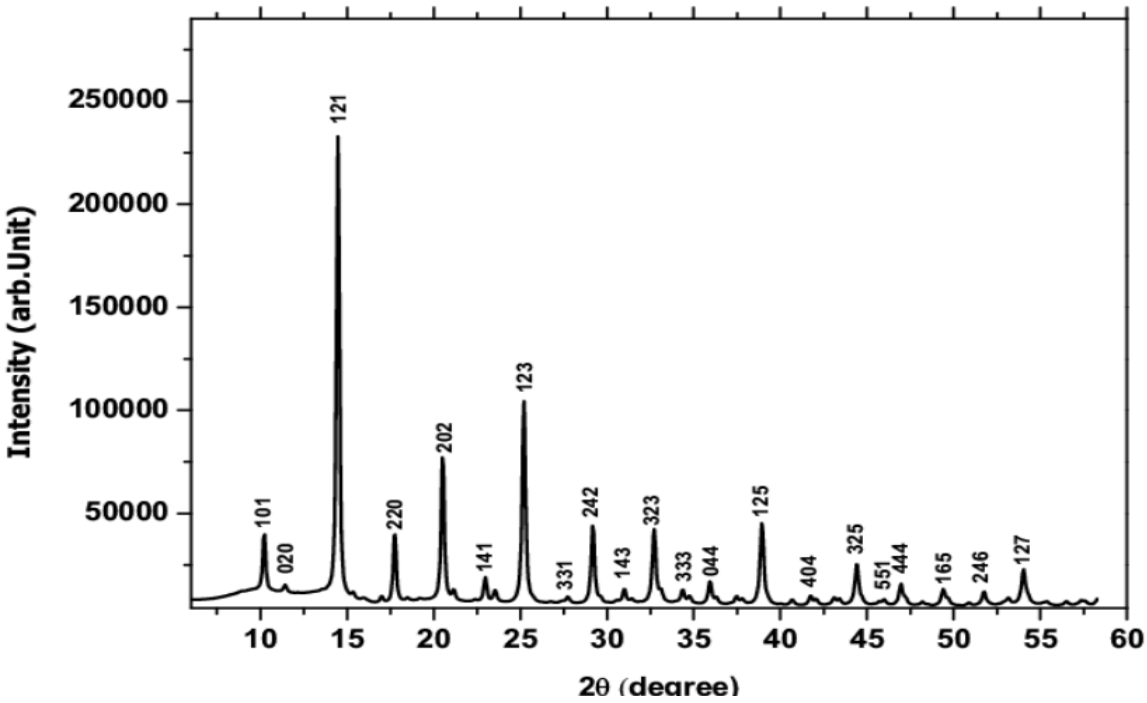

Fig. 1: Indexed room temperature synchrotron XRD pattern of $LaFeO_3$ prepared by a sol-gel auto-combustion method.

The crystallite size of the $LaFeO_3$ sample was calculated by the X-ray line broadening method using the Scherrer's formula: $D = k\lambda/\beta_D \cos\theta$ [32], where D is the crystallite size in nanometers, λ is the beam wavelength (λ = 0.7 Å), k is a constant equal to 0.94, β_D is the integral breadth, and θ is the peak position. The crystallite size was calculated by plotting $1/\beta_D$ on the x-axis and cosθ on the y-axis for orthorhombic $LaFeO_3$. The crystallite size D was calculated from the slope of the linear fit line, as shown in Fig. 2. Additionally, we used the Williamson-Hall method to calculate the average crystallite size and micro strain. Strain-induced broadening arising from crystal defects and distortion are related by

$$\varepsilon = \frac{\beta_s}{4\tan\theta} \tag{2}$$

The two equations presented below assume that the size and strain broadening represent the total integral breadth of a Bragg peak [33]. The theta dependences of the size and strain broadening in the Williamson-Hall analysis are described by the following equations:

$$\beta_{hkl} = \beta_\varepsilon + \beta_D = \left(\frac{K\lambda}{D\cos\theta}\right) + (4\varepsilon\tan\theta) \tag{3}$$

$$\beta_{hkl}\cos\theta = \left(\frac{K\lambda}{D}\right) + (4\varepsilon\sin\theta) \tag{4}$$

The $\beta_{hkl}\cos\theta$ term was plotted against 4sinθ for the orthorhombic perovskite $LaFeO_3$ to obtain the strain component from the slope (ε) and the average crystallite size component from the intercept ($K\lambda/D$), as shown in Fig. 3. The crystallite size of the as-prepared powder was found to be approximately 20.4 ± 1 nm.

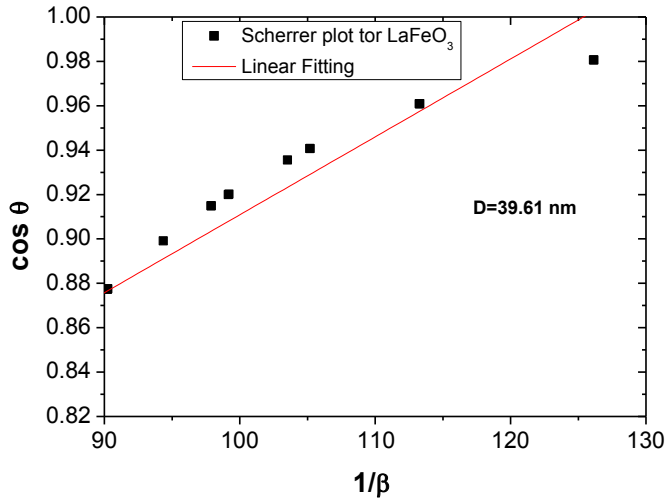

Fig. 2: Scherrer's plot of the $LaFeO_3$ perovskite. The crystalline size D is calculated from the slope of the linear fit.

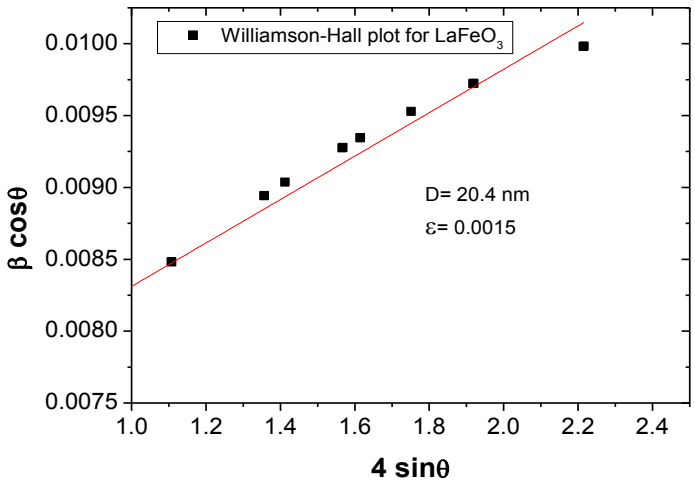

Fig. 3: Williamson-Hall plot for the $LaFeO_3$ perovskite. The crystallite size of the as-prepared powder is found to be approximately 20.4 ± 1 nm.

4.2. XRD Data Refinement

The FullProf program was used for Rietveld analysis of the synchrotron XRD data of $LaFeO_3$. Refinements were performed in the SG Pnma. In each refinement, a total of more than twenty parameters were refined: zero shift, scale factor, background coefficients, lattice parameters, asymmetric parameters, oxygen parameters for the isotropic temperature factor, and full width at half maximum.

The Rietveld plot of the refinements for the prepared $LaFeO_3$ is shown in Fig. 4. The observed intensity data are plotted in the upper section as points. The calculated intensities are shown in the same section as the black curve. The difference between the observed and calculated intensities is shown in the lower section (blue line). The short vertical bars in the center of the plot show the Bragg positions.

We considered different possible spin magnetic orderings at the Fe^{3+} sites in the $LaFeO_3$ structure and found that the ground state corresponds to an antiferromagnetic G-type ordering, as shown in Fig. 5, which agrees

with the experimentally reported antiferromagnetic ordering at a Néel temperature of T_N = 747 K [34]. Furthermore, the calculated Fe–O–Fe bond angles and the Fe–O bond lengths are displayed in Table 2.

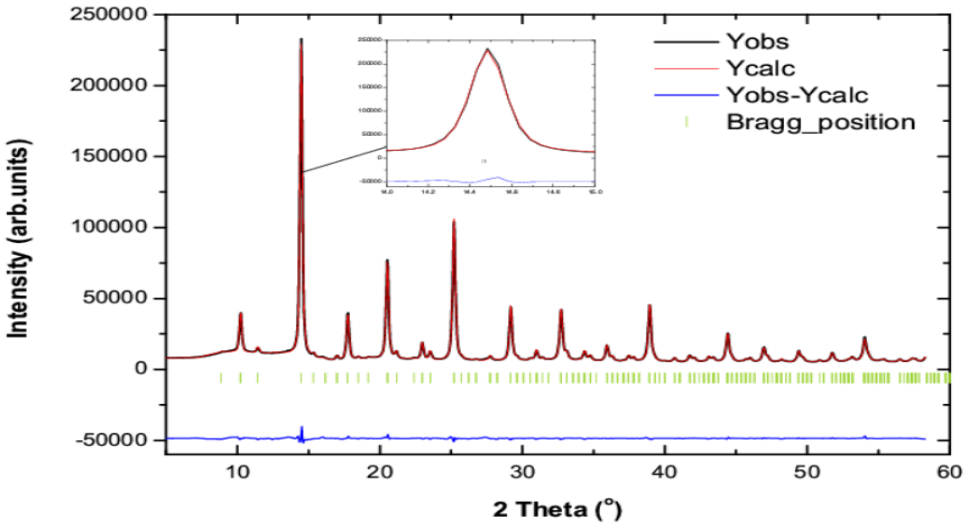

Fig. 4: The profile fitting for orthorhombic $LaFeO_3$ of space group Pnma.

Atomic coordinates, the site occupancy factor (SOF) for each cation in the A and B sites, the residual errors, and the refined lattice parameters for the orthorhombic $LaFeO_3$ perovskite with the SG Pnma are displayed in Table 1.

Table 1. Atomic coordinates, SOF for each cation in the A and B sites, R factors, equivalent thermal parameters, and refined lattice parameters for the orthorhombic $LaFeO_3$ perovskite with SG Pnma.

Atom label	Wyckoff Positions	Atomic coordinates			SOF
		x	*y*	*z*	
La	**4c**	0.02493	0.25000	0.99615	0.49524
Fe	**4b**	0.00000	0.00000	0.50000	0.50702
O1	**4c**	0.48288	0.25000	0.08164	0.48892
O2	**8d**	0.28163	0.46142	0.71871	1.10338

α=β= γ=90°		R_{exp}	1.82
a/Å	5.5575	R_{wp}	4.79%
b/Å	7.8512	R_p	4.59%
c/Å	5.5534	χ^2	6.93
V/Å^3	242.31	R-factor	1.75%
a/b	0.7078	RF-factor	1.28%
c/b	0.7073	GoF	2.28

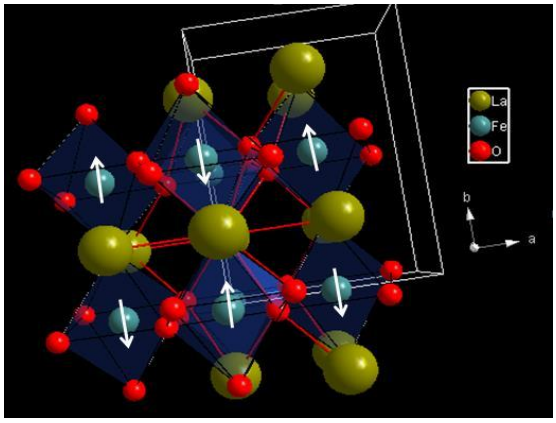

Fig. 5: Molecular structure of $LaFeO_3$ showing the FeO_6 and LaO_4 octahedra with G-type antiferromagnetic spin ordering indicated by the up and down arrows at the Fe sites.

4.3. Electron Density Calculations

Among the important results achieved by the Rietveld refinement includes the electron density calculated using the GFourier program, which is used to calculate and visualize the electron density inside the unit cell. This visualization is very valuable in identifying the atomic positions of the constituent elements within the unit cell for known or unknown crystals, i.e., a denser electron density contour indicates the position of a heavier element among the essential elements in the unit cell. The scattering density ρ(x,y,z) is typically calculated according to the equation:

$$\rho(x,y,z)=\frac{1}{V}\sum_{hkl}\left|F_{hkl}\right| e^{\{-2\pi i(hx+ky+lz-\alpha_{hkl})\}} \quad (5)$$

where ρ(x,y,z) is the electron density at a point x,y,z in the unit cell of volume V, F_{hkl} is the structure factor amplitude, and α_{hkl} is the phase angle of each Bragg reflection (h,k,l).

Electron density maps may then be visualized as either a two- or three- dimensional (2-D or 3-D) Fourier map. 2-D maps are classically drawn with contours (and sometimes colors) to indicate different density levels, while 3-D maps employ a chicken-wire style signifying a single level. The 2-D maps of the plane x = 0 in $LaFeO_3$ were successfully calculated using the GFourier program in the FullProf package.

The zero-level density contour is shown in black, while the colored regions of red to violet-brown indicate increasing levels of electron density around the La cation. Relatively large displacements in the various oxygen positions in the unit cell are observed compared to the Fe and La positions, where strong positive peaks correspond to the 4c sites. In the structure, the cations Fe and La are located at 0, 0, 1/2 and 0.028, 0.25, 0.993, respectively. The difference in the scattering density between the oxygen anion and La and Fe cations is very marked and shown in Fig. 6(a, b).

Fig.7 shows a 3-D Fourier map corresponding to the $x = 0$ section, where strong positive peaks corresponding to the 4c sites for the La^{3+} cations (A site) are observed, and some intermediate nuclear density is observed between both peaks corresponding to the 4b sites for the Fe^{3+} cations (B site).

Table 2. Calculated axial, equatorial bond lengths and angles between the cations of orthorhombic $LaFeO_3$.

Atom 1	Atom 2	Symmetry op. 2	d 1,2 [A]	Atom 3	Symmetry op. 3	d 1,3 [A]	Angle 2,1,3 [°]
La1	O1	-0.5+x, 0.5-y, 0.5-z	2.4296(90)	O2	-0.5+x, y, 0.5-z	2.4397(67)	114.504(119)
La1	O2	-0.5+x, y, 0.5-z	2.4397(67)	O2	-0.5+x, 0.5-y, 0.5-z	2.4397(67)	85.662(180)
Fe2	O2	x, y, z	2.0016(50)	O2	-x, -y, 1-z	2.0016(50)	180
Fe2	O1	-0.5+x, 0.5-y, 0.5-z	1.9940(193)	Fe2	-x, -0.5+y, 1-z	3.9187	169.306
Fe2	O1	-0.5+x, 0.5-y, 0.5-z	1.9940(193)	Fe2	0.5-x, -y, -0.5+z	3.9250	86.492
Fe2	O1	-0.5+x, 0.5-y, 0.5-z	1.9940(193)	Fe2	0.5-x, -y, 0.5+z	3.9250	100.093
Fe2	O2	x, y, z	2.0016(50)	O2	0.5-x, -y, -0.5+z	2.0166(50)	91.149(203)
Fe2	O2	-x, -y, 1-z	2.0016(50)	O1	0.5-x, -y, 0.5+z	2.0053(13)	89.874(178)
Fe2	O1	-0.5+x, 0.5-y, 0.5-z	2.0053(13)	O1	0.5-x, -y, 0.5+z	2.0053(13)	180
Fe2	O1	-0.5+x, 0.5-y, 0.5-z	2.0053(13)	O2	-0.5+x, y, 1.5-z	2.0166(50)	89.136(177)
Fe2	O1	-0.5+x, 0.5-y, 0.5-z	2.0053(13)	O2	0.5-x, -y, -0.5+z	2.0166(50)	90.864(177)
Fe2	O1	0.5-x, -y, 0.5+z	2.0053(13)	O2	-0.5+x, y, 1.5-z	2.0166(50)	90.864(177)
Fe2	O1	0.5-x, -y, 0.5+z	2.0053(13)	O2	0.5-x, -y, -0.5+z	2.0166(50)	89.136(177)
Fe2	O2	-0.5+x, y, 1.5-z	2.0166(50)	O2	0.5-x, -y, -0.5+z	2.0166(50)	180
O1	Fe2	0.5-x, -y, -0.5+z	2.0053(13)	Fe2	0.5+x, 0.5-y, 0.5-z	2.0053(13)	156.760(2)
O2	Fe2	x, y, z	2.0016(50)	Fe2	0.5-x, -y, 0.5+z	2.0166(50)	156.386(280)

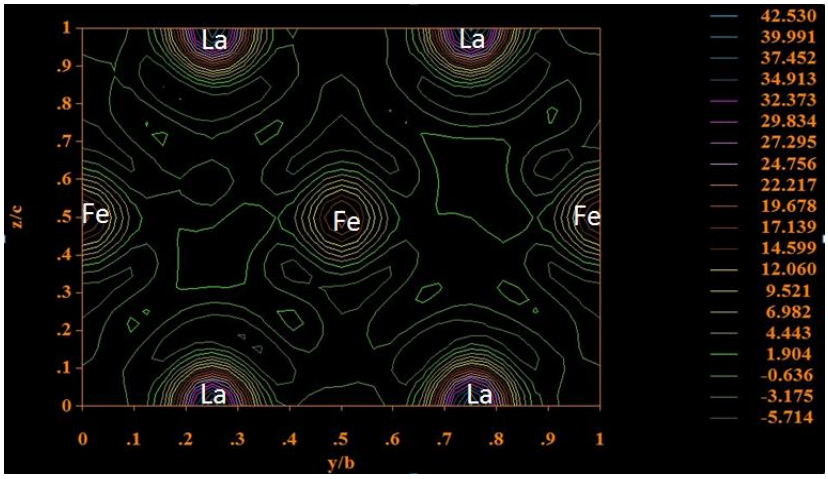

Fig. 6 (a): 2-D electron density map of individual atoms at z=0 in the unit cell of the $LaFeO_3$ perovskite using the GFourier program in the FullProf software package. The electron density is measured in electrons per cubic angstrom, e $Å^{-3}$.

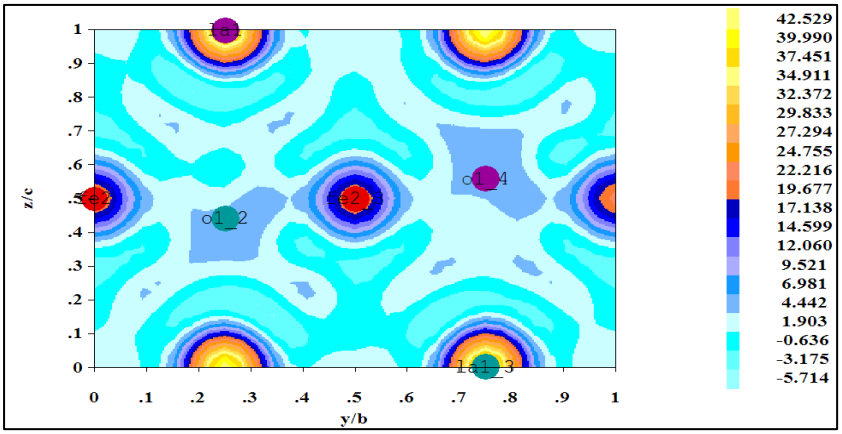

Fig. 6 (b): The maximum entropy method (MEM) map of valence electron density distribution in the yz plane of the full unit cell of $LaFeO_3$.

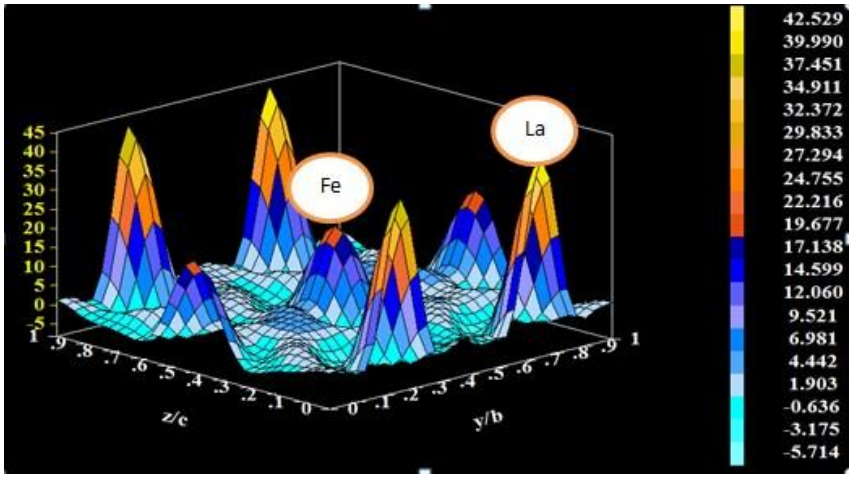

Fig. 7: 3-D contour map of the electronic density of individual atoms in the unit cell of $LaFeO_3$ at x=0.0. La peaks are clearly located at the 4c sites.

4.4. TEM analysis

TEM is the main technique used to characterize the microstructure of nanocrystalline materials (crystallite size and particle shape) [35].

Selected-area electron diffraction (SAED) and micro-diffraction patterns of a crystal were used to obtain the symmetry of the lattice and to calculate its interplanar distances.

According to the room temperature synchrotron XRD results (Fig. 1), the single-phase noncrystalline material consists of many tiny single crystals. The diffraction pattern of the prepared sample will therefore appear as a superposition of the single-crystal spotty patterns and display a series of concentric rings, resulting from several spots near each other at several rotations around the central beam spot. Each ring represents a reflection of planes with different interplanar spacing.

The HRTEM image recorded from the tip of the individual semi-spherical $LaFeO_3$ particle with an average crystallite size of 22±1.05 nm is shown in Fig. 8(a). Fig. 8(a,b,c) shows that the particles consist of an agglomeration of numerous nanocrystallite particles with semi-spherical shapes, and the unidirectional alignment of the lattice fringes confirmed the polycrystalline nature. The dissimilar values of the particle size investigated by TEM and XRD techniques result from the agglomeration of the $LaFeO_3$ sample particles. The HRTEM image of the prepared perovskite shows lattice planes with an interplanar spacing of 0.24 nm, corresponding to the (121) crystallographic plane of orthorhombic $LaFeO_3$, as indicated in Fig. 8(c,d). The alternate bright and dark regions in the HRTEM image signify the variation in surface thickness of $LaFeO_3$ nanospheres, as shown in Fig. 8(b).

The corresponding SAED pattern shown in Fig. 9 indicates its polycrystalline nature, resulting from diffraction of the nanoparticles. Therefore, by combining this result with the HRTEM profile, the observed results are in good agreement with the XRD results and Rietveld analysis.

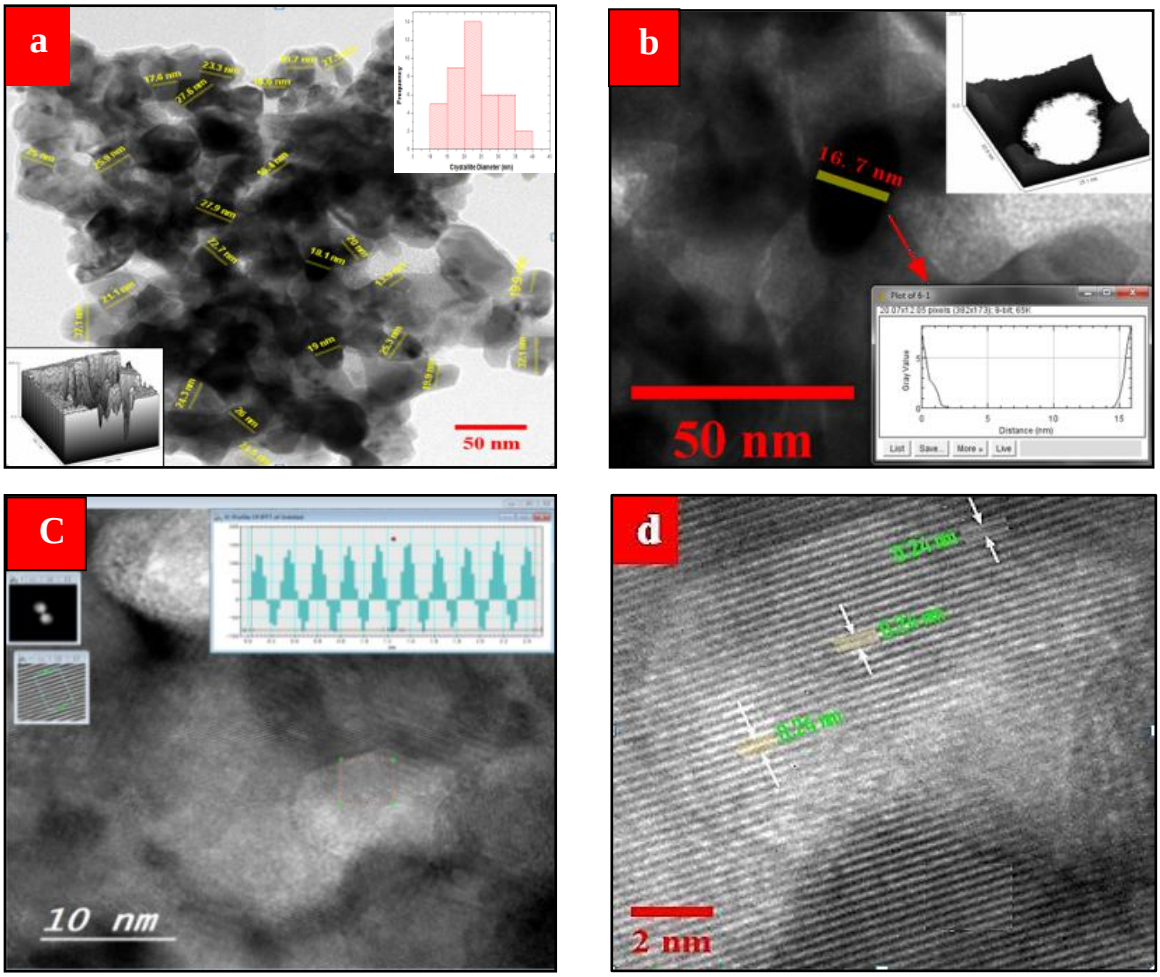

Fig. 8(a, b): HRTEM images of the nanospherical $LaFeO_3$ morphology. (c, d) Corresponding SAED lattice pattern with an interplanar spacing of 0.24 nm corresponding to plan (101).

The diffraction rings are discontinuous and consist of sharp spots, indicating the good crystallinity of the $LaFeO_3$ nanospheres, as shown in the SAED pattern in Fig. 9. The major diffraction spots correspond to the (101), (121), (220) and (202) planes of orthorhombic $LaFeO_3$, without any spots related to impurity phases, which is consistent with the XRD results. The patterns were indexed using C Spot (Trial version 2.0). The diffraction profiles created from the ring diffraction pattern can be viewed as equivalents of the XRD.

The diffraction rings are discontinuous and consist of sharp spots, indicating the good crystallinity of the $LaFeO_3$ nanospheres, as shown in the SAED pattern in Figure 14. The major diffraction spots correspond to the (101), (121), (220) and (202) planes of orthorhombic $LaFeO_3$, without any spots related to impurity phases, which is consistent with the XRD results. The patterns were indexed using C Spot (Trial version 2.0). The diffraction profiles created from the ring diffraction pattern can be viewed as equivalents of the XRD.

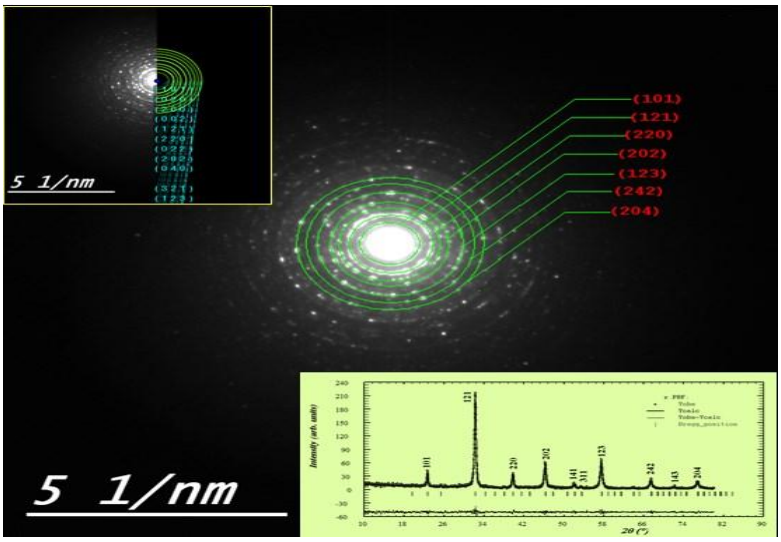

Fig. 9: SAED patterns of the $LaFeO_3$ perovskite (indexed using C Spot program).

4.5. Magnetic Measurements

The magnetic hysteresis loops were characterized to determine the saturation magnetization (Ms), remnant magnetization (Mr) and coercivity (Hc). The hysteretic behavior through the M(H) loop of the $LaFeO_3$ perovskite was characterized at room temperature by VSM in the field range of ±20 kOe. The magnetic properties of the sample were characterized by a VSM in a field of 15 kOe from room temperature to 800 K. The Curie temperature determined by the M (T) curve is approximately 730 K, as shown in Fig. 10. The hysteresis loop for nano-sized $LaFeO_3$ is shown in Fig. 11.

The $LaFeO_3$ perovskite is known to display antiferromagnetic and insulator behavior at room temperature, as previously mentioned [36]. However, the M (T) and M (H) curves of the prepared perovskite show weak ferromagnetic behavior. The M (H) curve confirms weak ferromagnetism with the highest magnetization (M) at 20 kOe of ~1.7566 emu/g and HC of ~125 Oe. This might be caused by antiferromagnetic ordering with canted spins [37]. Therefore, the room-temperature ferromagnetism in the investigated sample can be described by the supper exchange (SE) interaction of the Fe^{3+}–O^{2-}–Fe^{3+} ions, which induces a ferromagnetic shell model at the surface of a particle due to disordered spins, while an antiferromagnetic core is induced due to ordered spins [38, 39].

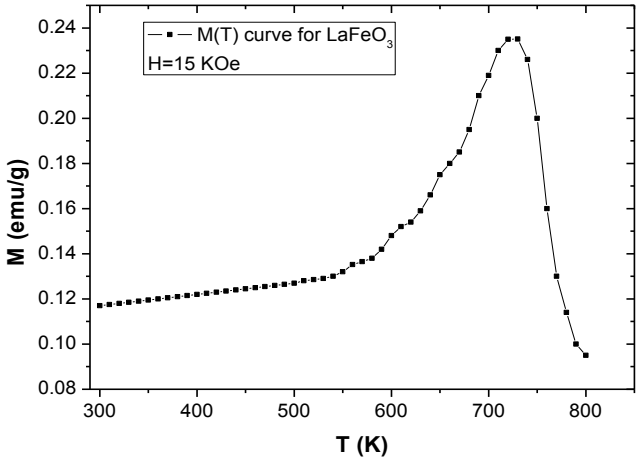

Fig. 10: M (T) curve of the orthorhombic $LaFeO_3$ Perovskite at a field of 15 KOe.

This behavior indicated an increasing ratio of the volume fractions of disordered spins to ordered spins of the Fe^{3+} ions with a decreasing crystallite size, in addition to a high surface area, resulting in an increased magnetic interaction. This behavior has also been detected in other types of perovskite structures [40].

The parameters from the hysteresis loop obtained from VSM for the $LaFeO_3$ perovskite are summarized in Table 3. Furthermore, during heating of the sample, some coupled Fe^{3+}-Fe^{2+} ions may appear in $LaFeO_3$ due to the loss of oxygen [41]. The difference between the magnetic moments of the Fe^{3+} (5 μB) and Fe^{2+} ions (4 μB) contributes to the magnetic behavior of the prepared $LaFeO_3$ sample.

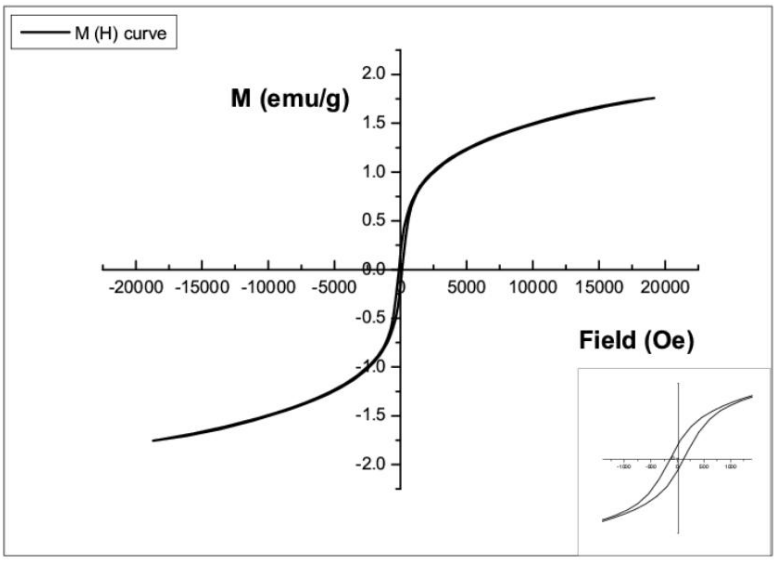

Fig. 11: Room-temperature M (H) curve of nano-sized $LaFeO_3$ in the field range of ±20 KOe.

Table 3. Magnetic parameters obtained from the M (H) curve for the prepared $LaFeO_3$ perovskite.

Hci (Oe)	Ms (emu/g)	Mr (emu/g)	Slope at Hc (emu/(g Oe)	R=Mr/Ms	H_{C+} (Oe)	H_{C-} (Oe)	H_{EX} (Oe)
125	1.7566	0.1669	0.0013	0.095	125.03	124.9	0.02

If the prepared nano-sized powder has some particles with multiple domain sizes, Hc, Mr, and R will deviate from zero. A larger particle size will give a higher R with a more apparent ferromagnetic behavior. Thus, we suggested that the ratio R = Mr/Ms could be used as a parameter to assess the homogeneity on the nanoparticle dimensions and the maximum limit of the single domain size of the magnetic nano-sized powder material. As stated above, the prepared nano-sized $LaFeO_3$ powder is weakly ferromagnetic, which indicates that Mr≠ 0.

This material is a multidispersed system consisting of single-domain and multiple-domain particles. The magnetization is overestimated at finite temperatures primarily because of a failure to account for magnetization suppression due to thermally excited collective spin-wave excitations. Therefore, the sample magnetization is considered as the sum of two terms:

$$M(H) = M_{sp}(H) + M_f(H) \quad (6)$$

where Msp(H) is the contribution of the superparamagnetic (sp) nanoparticles (single domain), and M_f(H) is the contribution of the ferromagnetic (f) nanoparticles (multiple domains):

$$M^{f}(H)=\frac{2M_s^{f}}{\pi}\tan^{-1}\left[\frac{H\pm H_c}{H_c}\tan(\frac{\pi R}{2})\right] \quad (7)$$

where μ_s^f is the saturation magnetization of the ferromagnetic phase and R is the rectangular coefficient of the ferromagnetic hysteresis loop.

The magnetization of the superparamagnetic mono-disperse $LaFeO_3$ nanoparticles above the blocking temperature T_B can be expressed as:

$$M(H)=M_S L[x] \quad (8)$$

where Ms=Nμ is the saturation magnetization for N nanoparticles with magnetic moment μ, and L(x) = cot(x)-1/x is the Langevin function, where x= μH/k_BT [42]. The magnetization of the superparamagnetic (sp) phase of the $LaFeO_3$ nanoparticles is given by the formula:

$$M^{sp}(H)=M^{sp}(\infty)\sum_j f(\mu_j)L\left[\frac{\mu_j H}{K_B T}\right] \quad (9)$$

where μ_j is the magnetic moment of the particle, and $f(\mu_j)$ is the weighted term of the Langevin function [43]. The magnetic moment (μ) and particle diameter (d) are related by the following:

$$\mu = M_S\, d^3\, \pi/6 \quad (10)$$

By using the above equations, we calculated the size of the nanoparticles by fitting the M(H) curve (at 27 ^{o}C) with the Langevin function for the $LaFeO_3$ perovskite, as shown in Fig. 12.

Fig. 13 shows the variation of the inverse molar magnetic susceptibility (χ_M) with the absolute temperature at a magnetic field of 1.5 KOe in the temperature range of 500-850 K for the $LaFeO_3$ perovskite. Clearly, χ_M decreases with an increasing temperature. Some antiferromagnetism and even some local magnetic phase separation can exist, which results in a decreased magnetization.

To further illustrate this behavior, the Cuire-Weiss formula was used to analyze the 1/χ versus T curve for the prepared $LaFeO_3$, as shown in Fig. 13.

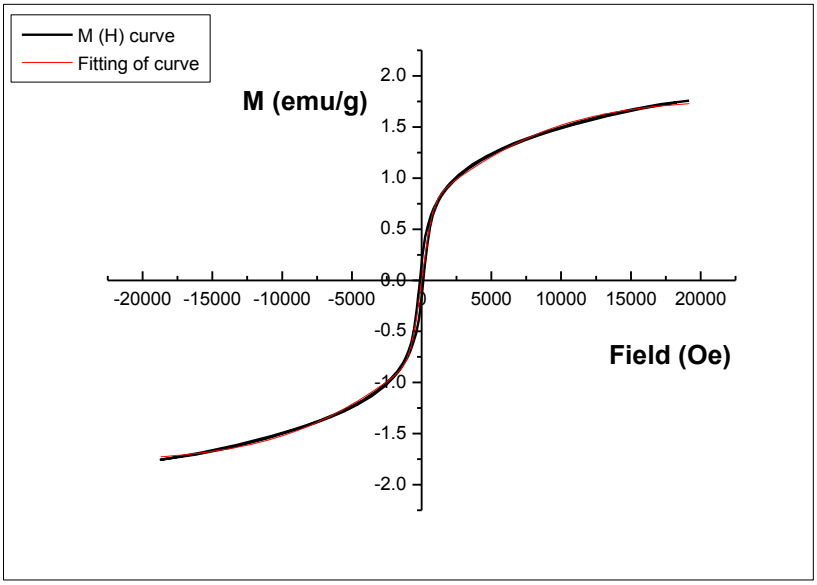

Fig. 12: Hysteresis curve fitted by the Langevin function for $LaFeO_3$. The Langevin function fitting obtained an average diameter d=22.4± 0.16 nm.

The susceptibility of the ferromagnetic material is described as follows:

$$\chi = \frac{C}{T-\theta} = \frac{M}{H} = \frac{N_A \mu_{eff}^2 \mu_B^2}{3KT} \quad (11)$$

where $C = N_A \mu_B^2 \mu_{eff}^2 / 3k_B$ is the Curie constant, N_A is Avogadro's number, μ_B is the Bohr magneton, $\mu_{eff} = \mu_B \, g\sqrt{S(S+1)}$ is the effective magnetic moment, g=2 is the gyromagnetic ratio, S is the magnetic spin, k_B is the Boltzmann constant, and θ is the paramagnetic Weiss temperature.

The Curie constant and effective magnetic moment was calculated from the linear fitting of the 1/χ vs T plot using the following relationships:

$$C = \frac{1}{\text{slope}}, \quad \mu_{eff} = \sqrt{\frac{3K_B C}{\mu_B N_A}} = 2.83\sqrt{C} \quad (12)$$

The θ value was calculated from the intercept of the linear fit with the temperature axis. The data are reported in Table 4, where θ is positive, indicating the ferromagnetic behavior of the prepared $LaFeO_3$ perovskite.

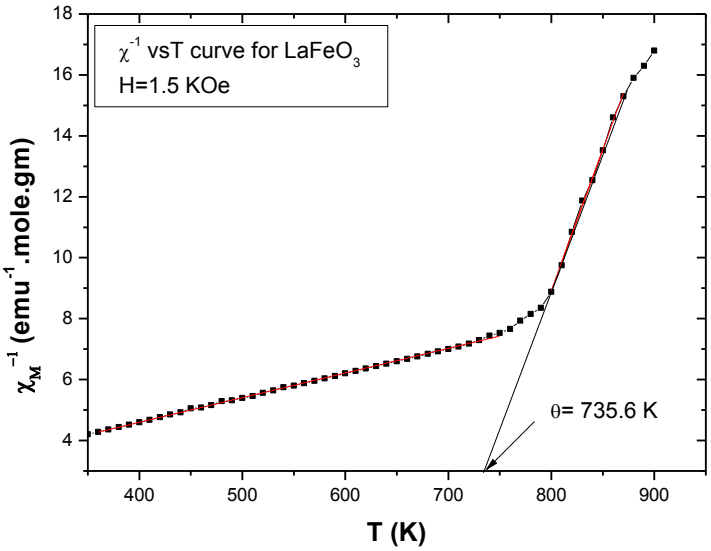

Fig. 13: Temperature dependence of the inverse molar susceptibility for $LaFeO_3$ at a field of 1.5 KOe.

The exchange coupling between close neighbors results in parallel arrangement of the magnetization in ferromagnetic materials. According to the Heisenberg Hamiltonian representation, the exchange coupling between nearest spins can be described as follows:

$$E_{ex} = -2J \, S_i \cdot S_j = -2J \, S_i S_j \cos\theta \quad (13)$$

where J is the exchange integral, and S_i and S_j are the two closest neighboring spins. The sign of the exchange integral determines whether the system has ferromagnetic or antiferromagnetic coupling.

For ferromagnetic materials, J is positive. Finding a way to reveal the relationship between the Curie temperature and the exchange integral is challenging for our prepared $LaFeO_3$ perovskite. According to Bethe and Slater [44], when the interatomic distance is small, the electrons spend the majority of their time between neighboring atoms, resulting in an increased antiparallel alignment and thus a negative J (antiferromagnetism). If the atoms are distant, the electrons spend the majority of their time away from each other to minimize electron repulsion, leading to parallel arrangement and thus a positive exchange J (ferromagnetism).

We assume that the exchange interaction operated only over "Z" (the number of molecules per unit cell), possessing a value of "J_{ex}". The Weiss field theory was used to determine the exchange integral J_{ex}, from the equation below, which defines the relationship between the exchange interaction constant J_{ex} and the Curie temperature T_C in ferromagnets:

$$J_{ex} = \frac{3\,K_B T_C}{2\,Z\,S(S+1)} \qquad (14)$$

where S is the spin (S = 5/2 for an Fe^{3+} ion). The J value was represented as J/k_B and is reported in Table 4. The exchange interaction (J_{33}) is believed to be negative and strong between trivalent Fe ions. The possible existence of a small number of Fe^{2+} ions arising from the preparation could create another type of exchange interaction, namely, J_{22} and J_{23}, which are expected to be negative and positive characteristics, respectively.

Table 4. Curie temperature, Curie constant (C), Curie-Weiss constant (θ), effective magnetic moment μ_{eff}, and exchange interaction constant (J/k_B) for the prepared perovskite.

C [(e.m.u/g).mol.$K^{]-1}$	μ_{eff} (B.M)	θ (K)	T_c (K)	J_{ex}/K_B
10.83	9.31	735.60	730	31.29

5. Conclusions

$LaFeO_3$ nanoparticles were successfully synthesized through a sol-gel auto-combustion method using citric acid as a fuel. Structural analysis showed that the structure consisted of a single phase of orthorhombic $LaFeO_3$ in the SG Pnma. The HRTEM image recorded from the tip of the individual semi-spherical particles revealed an average particle size of 22±1.05 nm. The observed HRTEM results were in good agreement with the XRD results and Rietveld analysis. The SAED patterns of the investigated $LaFeO_3$ showed spotty ring patterns, signifying the formation of a polycrystalline orthorhombic structure .

The electron density map and MEM showed an increase in electron density around the La cations (A site) and relatively large displacements in the various oxygen positions in the unit cell compared to the Fe and La positions, where strong positive peaks corresponded to the 4c sites.

The room-temperature magnetic properties measurements showed that the $LaFeO_3$ perovskite sample with an average particle size of 22.4± 0.16 nm exhibited soft ferromagnetic behavior with magnetization in the range of ±20 kOe of ~1.75 emu/g. This behavior indicated that ferromagnetism resulted from uncompensated spins at the surface and canted spin, which is the nature of size-induced magnetism for nanoparticles.

The positive paramagnetic Weiss temperature indicating the ferromagnetic behavior of the prepared $LaFeO_3$ perovskite.

ACKNOWLEDGMENTS

The authors acknowledge the support provided by IUPAP-IUCr LAAMP within the ICSU Grants Programme 2016-2019. We would like to express special thanks for experimental assistance to Jasper Rikkert (MCX beamline scientist- Elettra synchrotron- Trieste- Italy) and Lara Gigli (postdoc in MCX beamline- Elettra synchrotron- Trieste- Italy).

REFERENCES

[1] J. Li, X. Kou, Y. Qin, H. He, J. Appl. Phys., vol. 92, Issue 12, pp. 7504-7509, (2002).

[2] M. B. Bellakki, V. Manivannan, Bull. Mater. Sci., vol. 33, Issue 5, pp. 611-618, (2010).

[3] D. Kuscer, M. Hrovat, J. Holc, S. Bernik, D. Kolar, J. Power Sources, vol. 61, Issue 1, pp.161-165, (1996).

[4] D. Fino, N. Russo, G. Saracco,V. Specchia, J. Catal., vol. 217, Issue 2, pp. 367-375, (2003).

[5] T. Selyama, N. Yamazoe, K. Eguchi, Ind. Eng. Chem. Prod. Res. Dev. vol. 24, Issue 1, pp. 19-27, (1985).

[6] D. Wang, X. Chu, M. Gong, Nanotech., vol. 17, Issue 21, pp. 5501-5505, (2006).

[7] G. Martinellia, M. C. Carotta, M. Ferroni, Y. Sadaoka, E. Traversa, Sens. Actuators B, vol. 55, pp. 99-110, (1999).

[8] V. Caignaert, A. Maignan, and B. Raveau, Solid State Commun., vol. 95, Issue 6, pp. 357–359, (1995).

[9] N. Gayathri, A. K. Raychaudhuri, and S. K. Tiwary, Phys. Rev. B, vol. 56, Issue 3, pp. 1345–1353, (1997).

[10] H. Taguchi, M. Nagao, and M. Shimada, J. Solid State Chem., vol. 97, Issue 2, pp. 476–480, (1992).

[11] M. A. Choudhury, S. Akhter, D. L. Minh, N. D. Tho, and N. Chau, J. Magn. Magn. Materials, vol. 272, PP. 1295–1297, (2004).

[12] K. Iwasaki, T. Ito, M. Yoshino, T. Matsui, T. Nagasaki, and Y. Arita, J. Alloys Comp., vol. 430, Issue 1-2, pp. 297–301, (2007).

[13] M.-H. Hung, M. V. M. Rao, and D.-S. Tsai, Mater. Chem. Phys, vol. 101, Issue 2-3, pp. 297-302, (2007).

[14] D. Bayraktar, F. Clemens, S. Diethelm, T. Graule, J. Van herle, and P. Holtappels, J. Eur. Ceram. Soc, vol. 27, Issue 6, pp. 2455–2461, (2007).

[15] G. A. Smolenskiiand, V. A. Bokov, J. Appl. Phys., vol. 35, Issue 3, pp. 915-918, (1964).

[16] T. M. Rearick, G. L. Catchen, J. M. Adams, Phys. Rev. B, vol. 48, Issue 1, pp. 224-238, (1993).

[17] A. Scholl, J. Stohr, J. Luning, J. W. Seo, J. Fompeyrine, H. Siegwart, J.P. Locquet, F. Nolting, S. Anders, E. E. Fullerton, M. R. Scheinfein, and H.A. Padmore, Science, vol. 287, Issue 5455, pp.1014-1016, (2000).

[18] S. E. Dann, D. B. Currie, M. T. Weller, M. F. Thomas, A. D. Al-Rawwas, J. Solid State Chem., vol. 109, Issue 1, pp.134-144, (1994).

[19] W. C. Koehler, E. O. Wollan, J. Phys. Chem. Solids, vol. 2, Issue 2, pp.100-106, (1957).

[20] M. Idrees, M. Nadeem, M. Atifc, M. Siddique, M. Mehmood, M.M. Hassan, Acta Mater., vol. 59, Issue 4, pp.1338-1345, (2011).

[21] N.W. Grimes, R.J. Hilleard, J. Waters, J. Yerkess, J. Phys. C (Prog. Phys. Soc.), vol. 1, Issue 3, pp. 663-672, (1968).

[22] G. Blasse, Philips Res. Rep. Suppl., vol. 3, Issue 1, p.91, (1964).

[23] G.E. Bacon, F.F. Roberts, Acta Crystallogr., vol. 6, Issue 1, pp.57-62, (1953).

[24] M. Zhang, L. Yuan, X. Wang, H. Fan, X. Wang, X. Wu, H. Wang, Y. Qian, J. Solid State Chem., vol. 181, Issue 2, pp. 294-297, (2008).

[25] H. M. Rietveld, Acta Crystallogr., vol. 22, Issue 1, pp.151-152, (1967).

[26] H. M. Rietveld, J. Appl. Crystallogr. vol. 2, Issue 2, pp. 65-71, (1969).

[27] R. J. HILL, J. Appl. Crystallogr., vol. 25, Issue 5, pp. 589-610, (1992).

[28] S. Bid, S.K. Pradhan, J. Appl. Crystallogr. Vol.35, Issue 5, pp.517-525, (2002).

[29] S. Bid, S. K. Pradhan, Mater. Chem. Phys. vol. 82, Issue 1, pp. 27-37, (2003).

[30] H. Dutta, S.K. Manik, S.K. Pradhan, J. Appl. Crystallogr. Vol. 36, Issue 2, pp. 260-268, (2003).

[31] S. K. Manik, S. K. Pradhan, Mater. Chem. Phys., vol. 86, Issue 2, pp. 284-292, (2004).

[32] H. P. Klug and L. E. Alexander, "X-ray diffraction procedures for poly crystalline and amorphous materials," Second Edition, Wiley, (1974).

[33] M. Birkholz, Thin Film Analysis by X-ray Scattering. Wiley-VCH Verlag GmbH and Co. KGaA, Weinheim, (2006).

[34] C. Boekema, P. C. Jonker, G. Filoti and F. Van Der Woude, Hyperfine Interact. vol. 7, Issue 1, pp. 45–60, (1979).

[35] R. Grossinger, G. Badurek, J .Fidler, M. Zehetbauer, C. D. Dewhurst, J. Magn. Magn. Materials, vol. 294, Issue 2, pp. 152-185, (2005).

[36] S. Komine and E. Iguchi, J. Phys. Chem. Solids, vol. 68, Issue 8, pp. 1504–1507, (2007).

[37] A. V. Galubkov, E. V. Goncharova, V. P. Zhuze, and I. G. Manilove, Sov. Phys. Sol. State, vol. 7, Issue 8, pp. 1963–1967, (1966).

[38] E. A. Jaiswal, R. Das, K. Vivekanand, P. M.Abraham, S. Adyanthaya, P. Poddar, J. Phys. Chem. C, vol. 114, Issue 5, pp. 2108–2115, (2010).

[39] W. J. Schuele, V. D. Deetscreek, J. Appl. Phys., vol. 33, Issue 3, pp. 1136–1137, (1962).

[40] Y. Shimakawa, M. Azuma, and N. Ichikawa, J. Materials, vol. 4, Issue 1, PP. 153–168, (2011).

[41] N. T. Thuy and D. LeMinh, J. Adv. Mater. Scien. Engineering, vol. 2012, Issue 6, PP. 1-6 (2012).

[42] G. F. Goya, T. S. Berquo, and F. C. Fonseca, J. Appl. Phys., vol. 94, Issue 5, pp. 3520-3528, (2003).

[43] F. C. Fonseca, A. S. Ferlauto, F. Alvarez, G. F. Goya, and R. F. Jardim, J. Appl. Phys., vol. 97, Issue 4, pp. 04431371-04431372, (2005).

[44] A. Sommerfeld and H. Beterm, H. Geiger , K. Scheel (Eds) Handbuch der Physik, Berlin: Springer, vol. 24, Issue 2, p. 595, (1933).